

Revisiting XL-MIMO Channel Estimation: When Dual-Wideband Effects Meet Near Field

Anzheng Tang*, Jun-Bo Wang*, Yijin Pan*, Tuo Wu†, Yijian Chen‡,
Hongkang Yu†, and Maged Elkashlan§

Abstract—The deployment of extremely large antenna arrays (ELAAs) and operation at higher frequency bands in wideband extremely large-scale multiple-input-multiple-output (XL-MIMO) systems introduce significant near-field effects, such as spherical wavefront propagation and spatially non-stationary (SnS) properties. Combined with dual-wideband impacts, these effects fundamentally reshape the sparsity patterns of wideband XL-MIMO channels in the angular-delay domain, making existing sparsity-based channel estimation methods inadequate. To address these challenges, this paper revisits the channel estimation problem for wideband XL-MIMO systems, considering dual-wideband effects, spherical wavefront, and SnS properties. By leveraging the spatial-chirp property of near-field array responses, we quantitatively characterize the sparsity patterns of wideband XL-MIMO channels in the angular-delay domain, revealing global block sparsity and local common-delay sparsity. Building on this structured sparsity, we formulate the wideband XL-MIMO channel estimation problem as a multiple measurement vector (MMV)-based Bayesian inference task and propose a novel column-wise hierarchical prior model to effectively capture the sparsity characteristics. To enable efficient channel reconstruction, we develop an MMV-based variational message passing (MMV-VMP) algorithm, tailored to the complex factor graph induced by the hierarchical prior. Simulation results validate the proposed algorithm, demonstrating its convergence and superior performance compared to existing methods, thus establishing its effectiveness in addressing the challenges of wideband XL-MIMO channel estimation under complex near-field conditions.

Index Terms—Wideband XL-MIMO systems, dual-wideband effects, near-field effects, channel estimation, Bayesian inference.

I. INTRODUCTION

Wideband extremely large-scale multiple-input-multiple-output (XL-MIMO) has emerged as a pivotal technology to meet the capacity demands of future 6G communications [1], [2]. By exploiting the spatial degrees of freedom (DoFs) provided by extremely large antenna arrays (ELAAs), XL-MIMO significantly enhances both spectral and energy efficiencies [3]. It also delivers substantial beamforming gains, effectively mitigating the severe path loss characteristic of millimeter-wave (mmWave) frequencies. Additionally, the availability of GHz-wide bandwidth in the mmWave spectrum alleviates spectrum

A. Tang, J. Wang and Y. Pan are with the National Mobile Communications Research Laboratory, Southeast University, Nanjing 210096, China. (E-mail: {anzhengt, jbwang, and panyj}@seu.edu.cn)

T. Wu is with the School of Electrical and Electronic Engineering, Nanyang Technological University, 639798, Singapore (E-mail: tuo.wu@ntu.edu.sg).

Y. Chen and H. Yu are with the Wireless Product Research and Development Institute, ZTE Corporation, Shenzhen 518057, China. (E-mail: {yu.hongkang, chen.yijian}@zte.com.cn)

M. Elkashlan is with the School of Electronic Engineering and Computer Science, Queen Mary University of London, London E1 4NS, U.K. (E-mail: maged.elkashlan@qmul.ac.uk).

congestion, reinforcing the potential of mmWave XL-MIMO for next-generation wireless networks [4]. However, realizing these performance benefits critically depends on obtaining accurate channel state information (CSI), underscoring the importance of precise channel knowledge.

Typically, wideband XL-MIMO systems adopt orthogonal frequency division multiplexing (OFDM) to combat the frequency-selective fading of wireless channels [5]. However, due to the pronounced impact of dual-wideband effects, it is challenging to acquire accurate CSI. Specifically, the large system bandwidth shortens the OFDM symbol duration, potentially causing the propagation delay difference across the antenna array to exceed the symbol duration, leading to the spatial wideband effect [6]. Concurrently, the varying central frequencies of subcarriers introduce the frequency-wideband effect, where phase shifts differ across subcarrier channels, further complicating the channel estimation process.

Moreover, with the deployment of ELAAs and operation at higher frequency bands, near-field effects, such as the spherical wavefront effect [7]–[10] and spatially non-stationary (SnS) properties [11], [12], become prominent, exacerbating the dual-wideband effects. For instance, the sparsity structure of SnS dual-wideband XL-MIMO channels in the angular-delay domain undergoes significant changes. Specifically, the curvature of the spherical wavefront renders a single spatial frequency insufficient to characterize a near-field propagation path, requiring multiple spatial frequencies instead. This spatial frequency spread, combined with the frequency-wideband effect, amplifies angular spread compared to conventional massive MIMO systems [6], [13]. Additionally, the spherical wavefront effect disrupts the linear path delay variations across adjacent antennas, while SnS properties influence both spatial frequency and delay spreads. These combined factors reshape the sparse patterns of SnS dual-wideband XL-MIMO channels in the angular-delay domain, significantly complicating channel estimation in wideband XL-MIMO systems.

A. Related Works

Due to the limited scattering resulting from the highly directional propagation behavior of mmWave, mmWave channels typically exhibit significant sparsity. Consequently, most existing channel estimation methods are designed to exploit this inherent sparsity structure to simplify and improve the estimation process. For instance, leveraging the sparsity in the polar domain, various channel estimation and beam training schemes have been proposed to address the spherical effects in XL-MIMO channels [14]–[16]. Considering the inherent

spatial-domain sparsity induced by SnS properties, several Bayesian inference-based methods have been developed [17], [18] to mitigate the SnS effects. Additionally, exploiting the joint sparsity of XL-MIMO channels in both the spatial and angular domains, methods such as [8], [19] have proposed two-stage and joint VR detection and channel estimation algorithms, considering both spherical wavefront and SnS properties. However, despite these advancements, these methods predominantly focus on narrowband systems without the considerations of dual-wideband effects.

While some studies have explored wideband channels, such works remain limited in scope. For instance, [20] leverages the common polar-domain sparsity across subcarrier channels, employing the simultaneous orthogonal matching pursuit (SOMP) method for channel estimation. Nevertheless, as the bandwidth and array aperture increase in wideband XL-MIMO systems, the dual-wideband effects become more pronounced, challenging the assumption of common sparsity across subcarriers and diminishing the applicability of such methods.

Considering the sparsity differences among subcarriers, [13], [21] proposed methods that exploit subcarrier-dependent variations in sparsity patterns. Specifically, [13] recognized the sparsity-dependent pattern across subcarriers in dual-wideband channels and proposed jointly utilizing information from multiple subcarriers to enhance dual-wideband channel estimation performance. [21] developed a deep learning (DL)-based approach by unfolding the sparse Bayesian learning (SBL) algorithm into a deep neural network (DNN), where each SBL layer is carefully designed to capture subcarrier-dependent sparsity through a tailored variance parameter update mechanism. In addition, [22]–[24] developed the super-resolution-based estimation techniques to enhance performance by exploiting angular-delay domain sparsity. Unfortunately, these methods are tailored for far-field channels and cannot be readily extended to near-field scenarios due to the differences of sparsity patterns.

More recently, methods addressing both the spherical wavefront effect and dual-wideband effects have been proposed. For example, [25] introduced a bilinear pattern detection (BPD)-based approach to recover wideband XL-MIMO channels, while [26] developed a hybrid message passing algorithm based on constrained Bethe free energy minimization. However, despite these advancements, none of these approaches explicitly incorporate SnS properties, highlighting a significant gap in wideband XL-MIMO channel estimation.

B. Motivations and Contributions

Due to the randomness of the environment and user locations, spherical wavefront effects and SnS properties are inevitable in wideband XL-MIMO systems. However, the channel estimation problem that jointly considers the spherical wavefront effect, SnS properties, and dual-wideband effects has not been well addressed to date. Specifically, a well-established channel model for wideband XL-MIMO systems is lacking, and the sparsity patterns of these channels in the angular-delay domain have yet to be fully explored. Additionally, with the increasing number of antennas and subcarriers in XL-MIMO systems, there is a pressing need

for computationally efficient channel estimation algorithms to handle the growing complexity of these systems. To address these issues, this paper investigates channel estimation for XL-MIMO systems by incorporating the spherical wavefront effect, SnS properties, and dual-wideband effects. The main contributions of this paper are summarized as follows:

- To accurately characterize the SnS dual-wideband XL-MIMO channels, we derive a novel spatial-frequency domain model based on the measurement findings reported in [11], which comprehensively accounts for the spherical wavefront effect, SnS characteristics, and dual-wideband effects. By leveraging the spatial-chirp property of the array response, we quantitatively investigate the impact of the spherical wavefront effect, SnS properties, and dual-wideband effects on the angular and delay spreads. Furthermore, we reveal the sparsity patterns of SnS dual-wideband XL-MIMO channels in the angular-delay domain, incorporating both global block sparsity and local common-delay sparsity.
- Exploiting the sparsity of the angular-delay domain, the SnS dual-wideband XL-MIMO channel estimation is formulated as a multiple measurement vector (MMV)-based Bayesian inference problem. Recognizing the critical role of an accurate prior model in Bayesian inference, we propose a novel column-wise hierarchical prior model, where Markov random field (MRF) and common-delay sparsity mechanism is introduced to capture both the global block sparsity and the local common-delay sparsity, ensuring a more accurate and structured representation of the channel characteristics.
- To enable efficient Bayesian inference, we propose a MMV-based variational message passing (MMV-VMP) algorithm tailored for the column-wise hierarchical prior model. Unlike the variance states propagation algorithm in [27], which relies on first-moment matching methods under the mean-field approximation to update prior model parameters, the MMV-VMP algorithm employs structured variational inference combined with belief propagation. This approach effectively handles the higher-order dependencies and loops in the complex factor graph, ensuring precise and reliable message updates.
- Compared to existing methods, the proposed MMV-VMP algorithm achieves superior performance by jointly exploiting the global and common-delay sparsity of SnS dual-wideband channels in the angular-delay domain. Additionally, as the algorithm avoids matrix inversion operations, it maintains moderate computational complexity, making it well-suited for practical deployment in XL-MIMO systems.

C. Organization and Notations

The rest of the paper is organized as follows: Section II introduces the mmWave XL-MIMO system model. Section III develops a spatial-frequency channel model, incorporating spherical wavefront effects, SnS properties, and dual-wideband effects, and analyzes the angular-delay characteristics of SnS dual-wideband XL-MIMO channels. Section IV formulates the channel estimation problem as a sparse signal recovery task

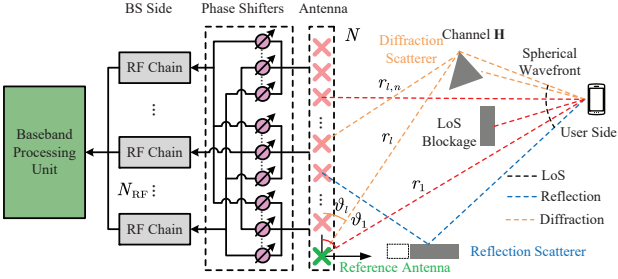


Fig. 1. Illustration of the XL-MIMO system model.

and proposes a column-wise hierarchical sparse prior model. Section V presents the MMV-VMP algorithm. Simulation results and conclusions are provided in Sections VI and VII, respectively.

Notations: lower-case letters, bold-face lower-case letters, and bold-face upper-case letters are used for scalars, vectors and matrices, respectively; The superscripts $(\cdot)^T$ and $(\cdot)^H$ stand for transpose and conjugate transpose, respectively; \odot denotes the Hadamard product; \mathbf{I}_n denotes a $n \times n$ identity matrix; $\mathbb{C}^{m \times n}$ denotes a $m \times n$ complex matrix. $\mathbf{1}_n$ denotes a $n \times 1$ all-one vector. In addition, a random variable $x \in \mathbb{C}$ drawn from the complex Gaussian distribution with mean x_0 and variance v is characterized by the probability density function $\mathcal{CN}(x; m, v) = \exp\{-|x - m|^2/v\}/\pi v$; a random variable $\gamma \in \mathbb{R}$ from Gamma distribution with mean a/b and variance a/b^2 is characterized by the probability density function $Ga(\gamma; a, b) \propto \gamma^{a-1} \exp(-\gamma b)$.

II. SYSTEM MODEL

Consider a mmWave XL-MIMO system, as shown in Fig. 1, where a base station (BS) utilizes an ELAA comprising N antennas arranged in a uniform linear configuration to serve a single-antenna user. To reduce hardware cost and energy consumption, the BS adopts a hybrid analog-digital architecture, where N_{RF} radio frequency (RF) chains are connected to the ELAA through phase shifters. The spacing between adjacent antennas is $d = \lambda_c/2$, where $\lambda_c = c/f_c$, with c and f_c indicating the speed of light and the central carrier frequency, respectively. In addition, to address frequency-selective fading, OFDM is utilized. Without loss of generality, assume that K subcarriers are uniformly selected from the available subcarriers to carry pilot symbols.

In this paper, we focus on the uplink channel estimation, where the BS combines the pilot signal using all RF chains associated with different beams. Let the total number of received beams be denoted by M , with M being an integer multiple of N_{RF} . Consequently, the BS requires $P = M/N_{RF}$ channel uses to cycle through all beams for a given pilot symbol. Denote $\iota_{k,p}$ as the pilot symbol of the k -th subcarrier in the p -th channel use. Then, the received signal for the k -th subcarrier in the p -th channel use can be expressed as

$$\mathbf{y}_{k,p} = \mathbf{W}_p \mathbf{h}_k \iota_{k,p} + \mathbf{n}_{k,p}, \quad (1)$$

where $\mathbf{W}_p \in \mathbb{C}^{N_{RF} \times N}$ denotes the combining matrix in the p -th channel use, with each entry adhering to a constant modulus constraint and independently generated from the set $\{-1/\sqrt{N}, 1/\sqrt{N}\}$; $\mathbf{h}_k \in \mathbb{C}^{N \times 1}$ denotes the spatial-domain channel vector for the k -th subcarrier, while $\mathbf{n}_{k,p} \sim$

$\mathcal{CN}(\mathbf{n}_{k,p}; \mathbf{0}, \beta^{-1} \mathbf{I}_{N_{RF}})$ represents the noise vector associated with the k -th subcarrier in the p -th channel use.

Assuming that all-one pilot symbols are adopted, i.e., $\iota_{k,p} = 1$ for all k and p , and collecting the pilot symbols across all P channel uses, the received signal for the k -th subcarrier can be written in a compact form as

$$\mathbf{y}_k = \mathbf{W} \mathbf{h}_k + \mathbf{n}_k, \quad (2)$$

where $\mathbf{W} = [\mathbf{W}_1^T, \mathbf{W}_2^T, \dots, \mathbf{W}_P^T]^T \in \mathbb{C}^{M \times N}$ and $\mathbf{n}_k = [\mathbf{n}_{k,1}^T, \mathbf{n}_{k,2}^T, \dots, \mathbf{n}_{k,P}^T]^T \in \mathbb{C}^{M \times 1}$ are the collective receive combining matrix and the effective noise vector, respectively. Furthermore, concatenating the received signals corresponding to different pilot subcarriers, the overall received signal $\mathbf{Y} = [\mathbf{y}_1, \mathbf{y}_2, \dots, \mathbf{y}_K] \in \mathbb{C}^{M \times K}$ is given by

$$\mathbf{Y} = \mathbf{W} \mathbf{H} + \mathbf{N}, \quad (3)$$

where $\mathbf{H} = [\mathbf{h}_1, \dots, \mathbf{h}_K] \in \mathbb{C}^{N \times K}$ and $\mathbf{N} = [\mathbf{n}_1, \dots, \mathbf{n}_K] \in \mathbb{C}^{M \times K}$ indicating the spatial-frequency channel matrix and effective noise matrix, respectively.

III. SNS DUAL-WIDEBAND XL-MIMO CHANNEL MODEL

In this section, we first derive a spatial-frequency channel model that incorporates the effects of spherical wavefront effect, SnS properties, and dual-wideband effects. Then, we quantitatively analyze the angular-delay characteristics of SnS dual-wideband XL-MIMO channels.

A. Channel Modeling for SnS XL-MIMO Systems

In XL-MIMO systems, the use of ELAA and high-frequency bands facilitates near-field communications over hundreds of meters, invalidating the far-field plane wavefront assumption and necessitating the consideration of spherical wavefront effects. Additionally, SnS properties arise as different array portions observe varying propagation conditions, causing power variations across array elements. Furthermore, dual-wideband effects in wideband XL-MIMO systems influence channel characteristics, requiring careful modeling.

Assume that there are L propagation paths between the BS and user. Denote $\mathcal{L} = \{1, 2, \dots, L\}$ as the set of all propagation paths, where $l = 1$ refers to the line-of-sight (LoS) path and $l > 1$ indicates reflection or diffraction path, as illustrated in Fig. 1. Denote $\tau_{l,n}$ as the time delay of the l -th path for the n -th antenna. Then the baseband channel impulse response of the n -th received antenna is given by

$$h_n(t) = \sum_{l=1}^L \tilde{\alpha}_l \kappa_{l,n} e^{-j2\pi f_c \tau_{l,n}} \delta(t - \tau_{l,n}), \quad (4)$$

where $\tilde{\alpha}_l \in \mathbb{C}$ denotes the complex path gain. $\kappa_{l,n}$ is introduced to characterize the SnS properties from the perspective of multipath propagation mechanisms, and it is given by [11]

$$\kappa_{l,n} \begin{cases} = 0, & n \notin \phi_l, \\ = 1, & n \in \phi_l \text{ \& LoS/Reflection,} \\ > 0, & n \in \phi_l \text{ \& Diffraction,} \end{cases} \quad (5)$$

$$h_n(f) = \int_{-\infty}^{+\infty} h_n(t) e^{-j2\pi f t} dt = \sum_{l=1}^L \alpha_l \kappa_{l,n} e^{-j2\pi(n\psi_l - n^2\varphi_l)} e^{-j2\pi f \tau_l} e^{-j2\pi f \left(n\frac{\psi_l}{f_c} - n^2\frac{\varphi_l}{f_c}\right)}. \quad (10)$$

where $\phi_l = [n_{l,s}, n_{l,e}]$ denotes the VR of the l -th path with $n_{l,s}$ and $n_{l,e}$ indicating the start and end index¹. Assume the distance and direction of the l -th path to the reference antenna element as r_l and ϑ_l , as illustrated in Fig. 1. Then, $\tau_{l,n}$, for any $l \in \mathcal{L}$, can be rewritten as

$$\tau_{l,n} = \tau_l + \frac{r_l - r_{l,n}}{c}, \quad (6)$$

where $\tau_l = r_l/c$; $r_{l,n}$ denotes the distance between the l -th scatterer and the n -th antenna element, which is defined as

$$\begin{aligned} r_{l,n} &= \sqrt{(r_l \cos \vartheta_l - nd)^2 + r_l^2 \sin^2 \vartheta_l} \\ &\stackrel{(a)}{\approx} r_l - nd \cos \vartheta_l + \frac{n^2 d^2}{2r_l} \sin^2 \vartheta_l. \end{aligned} \quad (7)$$

where (a) is obtained by using the Fresnel approximation, i.e., $\sqrt{1+x} \approx 1+x/2-x^2/8$. In this Taylor expansion, the current point is set at $n=0$, and terms of third order and higher are neglected. Utilizing (7), (6) can be rewritten as $\tau_{l,n} = \tau_l + n\psi_l/f_c - n^2\varphi_l/f_c$, where $\psi_l \triangleq d \cos \vartheta_l/\lambda_c$ and $\varphi_l \triangleq d^2 \sin^2 \vartheta_l/2r_l \lambda_c$. According to (6) and (7), the continuous time channel impulse response in (4) can be further expressed as

$$h_n(t) = \sum_{l=1}^L \alpha_l \kappa_{l,n} e^{-j2\pi(n\psi_l - n^2\varphi_l)} \delta(t - \tau_{l,n}), \quad (8)$$

where $\alpha_l \triangleq \tilde{\alpha}_l e^{-j2\pi f_c \tau_l}$ is the equivalent complex path gain. Applying the continuous time Fourier transform to (8), the spatial-frequency response of the n -th antenna is given by (10), as shown in the top of this page. Further, Eq. (10) can be expressed in a more compact form as

$$\mathbf{h}(f) = \sum_{l=1}^L \alpha_l a(f, \tau_l) (\kappa_l \odot \mathbf{b}(\psi_l, \varphi_l)) \odot \boldsymbol{\theta}(f, \psi_l, \varphi_l), \quad (11)$$

where $a(f, \tau_l) = e^{-j2\pi f \tau_l}$; $\kappa_l = [\kappa_{l,1}, \kappa_{l,2}, \dots, \kappa_{l,N}]^T$ denotes the visibility indicator vector with the n -th entry being $\kappa_{l,n}$; $\mathbf{b}(\psi_l, \varphi_l)$ and $\mathbf{a}(f, \tau_l)$ denote the array response vector and the frequency response vector, respectively, with each of their n -th entries given by

$$[\mathbf{b}(\psi_l, \varphi_l)]_n = e^{-j2\pi(n\psi_l - n^2\varphi_l)}, \quad (12)$$

$$[\boldsymbol{\theta}(f, \psi_l, \varphi_l)]_n = e^{-j2\pi f \left(n\frac{\psi_l}{f_c} - n^2\frac{\varphi_l}{f_c}\right)}. \quad (13)$$

Assuming the total bandwidth of the OFDM system is denoted by f_s , the center frequency for each subcarrier is given by $f_k = f_c + k f_s / K$ with $k = 0, 1, \dots, K$. The corresponding

¹For the diffraction paths, $\kappa_{l,n} \in \phi_l$ is associated with the diffraction coefficient. As such, $\kappa_{l,n}$ can be set within $0 < \kappa_{l,n} < 1$, with the reference value chosen as the element with the highest received power. Thus, we assume $\kappa_{l,n} \in \phi_l$ obeys a uniform distribution between 0 and 1. Additionally, we assume continuous VRs for simplicity. Notably, the proposed method is not restricted to continuous VRs and can be extended to scenarios involving disjoint VRs, where the visible antennas may be distributed across multiple disjoint regions for a specific path.

channel vector for each subcarrier is then represented as $\mathbf{h}(f_k)$, as illustrated in Eq. (11) with f replaced by f_k . Thus, the overall spatial-frequency channel matrix \mathbf{H} can be reformulated as

$$\mathbf{H} = \sum_{l=1}^L \alpha_l (\kappa_l \odot \mathbf{b}(\psi_l, \varphi_l)) \mathbf{a}^T(\tau_l) \odot \boldsymbol{\Theta}(\psi_l, \varphi_l). \quad (14)$$

where $\mathbf{a}(\tau_l) = [a(f_1, \tau_l), \dots, a(f_K, \tau_l)]^T$, and $\boldsymbol{\Theta}(\psi_l, \varphi_l) = [\boldsymbol{\theta}(f_1, \psi_l, \varphi_l), \dots, \boldsymbol{\theta}(f_K, \psi_l, \varphi_l)]$.

Remark 1. Eq. (14) presents a comprehensive channel model for XL-MIMO systems, integrating spherical wavefront effects, SnS properties, as well as spatial and frequency-wideband characteristics. Specifically, the spatial-domain steering vector $\mathbf{b}(\psi_l, \varphi_l)$ is coupled with the SnS indicator vector κ_l , the frequency response vector $\mathbf{a}(\tau_l)$, and the frequency-dependent phase matrix $\boldsymbol{\Theta}(\psi_l, \varphi_l)$. However, due to the high dimensionality of spatial-frequency channels in mmWave XL-MIMO systems, direct estimation becomes computationally prohibitive. Thus, it is essential to leverage channel sparsity in a suitable transform domain.

B. Angular-Delay Representation of SnS XL-MIMO Channel

Building on approaches used for traditional massive MIMO channels [6], the wideband XL-MIMO channels in (14) can be approximated as

$$\mathbf{H} \approx \mathbf{F}_A \mathbf{X} \mathbf{F}_D. \quad (15)$$

where $\mathbf{F}_A \in \mathbb{C}^{N \times N}$ and $\mathbf{F}_D \in \mathbb{C}^{K \times K}$ denote the normalized N - and K -dimensions DFT matrices. $\mathbf{X} \in \mathbb{C}^{N \times K}$ denotes the angular-delay channel.

Lemma 1. The angular-delay channel $\mathbf{X} = \mathbf{F}_A^H \mathbf{H} \mathbf{F}_D^*$ is a sparse matrix containing only L non-zero blocks, with the non-zeros elements staying inside a square region, i.e.,

$$\lim_{N, K \rightarrow \infty} [\mathbf{X}]_{n,k} = \begin{cases} \text{nonzeros}, & (n, k) \in \mathcal{A}_2, \\ 0, & (n, k) \notin \mathcal{A}_2, \end{cases} \quad (16)$$

where $\mathcal{A}_2 = \cup_{l,p} \mathcal{A}_{l,2,p}$ with

$$\begin{aligned} \mathcal{A}_{l,2,p} &= \{(n, k) \in \mathbb{Z}^2 \mid n = \text{mod}(n_l + N\epsilon_{l,p}, N), \\ &\quad k = \text{mod}(k_l + f_s \tau_l, K), \forall (n_l, k_l) \in \mathcal{A}_{l,1}\}, \end{aligned} \quad (17)$$

and $\text{mod}(a, m)$ is the modulus of a for m . In addition, $\epsilon_{l,p} = \psi_l - 2n_{l,e}\varphi_l + \eta_l(p-1)$ with $\eta_l = 2N\varphi_l/P$ and $p \in \{p \in \mathbb{N}^+ \mid \psi_l - 2n_{l,e}\varphi_l \leq \eta_l p \leq \psi_l - 2n_{l,s}\varphi_l\}$. $\mathcal{A}_{l,1} \triangleq \{(n_l, k_l) \in \mathbb{Z}^2 \mid I_{l,e} \leq n_l \leq I_{l,s}, J_{l,e} \leq k_l \leq J_{l,s}\}$ with $I_{l,e} = \min_k \lceil (i_{l,e}(k) + 1)N/2 \rceil$, $I_{l,s} = \max_k \lceil (i_{l,s}(k) + 1)N/2 \rceil$, $J_{l,e} = \min_n j_{l,e}(n)$, and $J_{l,s} = \max_n j_{l,s}(n)$, $\forall n \in \phi_l$, where

$$i_{l,e}(k) = 2(a_k - b_k n_{l,e}), \quad i_{l,s}(k) = 2(a_k - b_k n_{l,s}), \quad (18)$$

$$j_{l,e}(n) = (t_{l,n} - 2/K)K, \quad j_{l,s}(n) = (t_{l,n} + 2/K)K, \quad (19)$$

with $a_k = f_k \psi_l / f_c$, $b_k = 2f_k \varphi_l / f_c$, and $t_{l,n} = (n f_s \psi_l - n^2 f_s \varphi_l) / (K f_c)$.

From (17), the non-zero region of \mathbf{X} is synthesized from the shifted non-zero regions of $\mathbf{F}_A^H \Theta(\psi_l, \varphi_l) \mathbf{F}_D$ across angular and delay domains for all l . The shift distance are jointly determined by $N\epsilon_{l,p}$ and $f_s\tau_l$. In addition, The index of significant angular-delay components (n, k) within \mathcal{A}_1 and \mathcal{A}_2 form a parabolic shape, which arises because both $j_{l,e}(k)$ and $j_{l,s}(k)$ are quadratic functions of n .

Proof: Please see Appendix A.

Moreover, we analyze the effects of the spherical wavefront, SnS properties, and dual-wideband effects on the sparsity structure of \mathbf{X} based on Lemma 1 from the perspectives of the angular and delay spread. 1) **Angular Spread:** The spherical wavefront introduces angular spread of $\Theta(\psi_l, \varphi_l)$ in angular domain, ranging from $a_k - b_k n_{l,e}$ to $a_k - b_k n_{l,s}$ due to the inclusion of a quadratic term, $\varphi_l n^2$. Meanwhile, it affects the variations of $\epsilon_{l,p}$. The SnS properties influence the values of $n_{l,e}$ and $n_{l,s}$, thereby affecting the extent of the angular spread. Additionally, the frequency-wideband effect induces variations in $i_{l,e}(k)$ and $i_{l,s}(k)$ across subcarriers k , which further broadens the angular dispersion across the system bandwidth. 2) **Delay Spread:** The spatial-wideband effect causes variations in $j_{l,e}(n)$ and $j_{l,s}(n)$ across antennas n , leading to delay spread. The SnS properties define the range of variation for n , while the spherical wavefront imposes a quadratic trend on the delay spread as a function of n .

In summary, the spherical wavefront effect, SnS properties, and dual-wideband effects collectively influence the angular and delay spreads, reshaping the sparse patterns of SnS dual-wideband channels in the angular-delay domain, i.e.,

- **Global Block Sparsity:** The angular-delay channel contains L non-zero block corresponding to L propagation paths. The index range of each non-zero block is determined by $\mathcal{A}_{l,2}$.
- **Local Common-Delay Sparsity:** Due to the spherical wavefront effect, within \mathcal{A}_2 , different delay indices correspond to varying angular spreads, which occur in clusters and exhibit high correlation.

Remark 2. The global block sparsity and local common-delay sparsity arise from the combined effects of the spherical wavefront, SnS properties, and dual-wideband characteristics. These features inherently embed inter-antenna and inter-subcarrier correlations into the angular-delay channel. Furthermore, (15) offers an alternative representation of the spatial-frequency channel, facilitating the estimation of SnS dual-wideband XL-MIMO channels. Once the angular-delay channel is reconstructed, key parameters such as AoAs, VRS, and the range of beam squint can be efficiently extracted.

To enhance intuitive understanding of the SnS XL-MIMO channel, we provide an example with the following parameters: $N = K = 1024$, $f_s = 3\text{GHz}$, $f_c = 30\text{GHz}$, $r_l = 10\text{m}$, $\vartheta_l = \pi/5$, and $\phi_l \in [64, 959]$. Fig. 2 illustrates the block sparsity of the SnS XL-MIMO channel in the angular-delay domain. Given the specified parameters, we have $i_{l,e}(0) = 0.64$, $i_{l,s}(0) \approx 0.8$, $j_{l,e}(64) = 513$, and $j_{l,s}(64) \approx 517$. Similarly, $i_{l,e}(1023) \approx 0.88$, $i_{l,s}(1023) \approx 0.72$, $j_{l,e}(959) = 545$, and $j_{l,s}(959) \approx 549$. As depicted in Fig. 2(a) and Fig. 2(b), these values provide accurate boundaries for the ranges of angular

and delay spread. Additionally, the figures show that both the angular and delay spectra shift to the right due to $\cos\vartheta_l > 0$ and the monotonicity of t_n with respect to n .

Furthermore, we obtain the following values: $I_{l,e} = 841$, $I_{l,s} = 962$, $J_{l,e} = 513$, and $J_{l,s} = 549$. Fig. 2(c) illustrates the non-zero region of $\mathbf{F}^A \Theta(\psi_l, \varphi_l) \mathbf{F}_D^*$, which is accurately constrained to $\mathcal{A}_{l,1}$, validating the effectiveness of Lemma 1. Additionally, we have $f_s\tau_l = 100$, $\epsilon_{l,1} = \psi_l - 2n_{l,s}\varphi_l \approx 0.4$, and $\epsilon_{l,P} = \psi_l - 2n_{l,e}\varphi_l = 0.32$, corresponding to $N\epsilon_{l,1} = 410$ and $N\epsilon_{l,P} = 328$, respectively. Consequently, Fig. 2(d) and Fig. 2(e) represent shifted versions of Fig. 2(c). The shift distances in the angular domain are 696 and 614, respectively, while the shift distance in the delay domain is 100. Finally, by concentrating the shifted versions across all $\epsilon_{l,p}$, the sparse structure depicted in Fig. 2(f) is obtained. It can be observed that the angular range of $\mathcal{A}_{l,2}$ is broader than that of $\mathcal{A}_{l,1}$ due to the composite effect.

Remark 3. Compared to conventional massive MIMO-OFDM channels, the proposed SnS dual-wideband XL-MIMO channel exhibits distinct behavior. Specifically, in addition to beam squint, the spherical wavefront effect and SnS properties contribute to angular spread, resulting in broader angular diffusion. Moreover, the quadratic phase variations introduced by the spherical wavefront reshape the trend of delay variations across antennas. Notably, Lemma 1 is applicable to conventional MIMO-OFDM channels. When the spherical wavefront simplifies to a plane wavefront and SnS properties are disregarded, both φ_l and $\kappa_{l,n}$ can be omitted. Thus, (18) simplifies to $i_{l,e}(k) = i_{l,s}(k)$ and $t_{l,n} = n f_s \psi_l$. Consequently, the significant components are uniformly distributed within the non-zero region, as illustrated in [6].

IV. SNS DUAL-WIDEBAND CHANNEL ESTIMATION FOR XL-MIMO SYSTEMS

In this section, leveraging the sparsity outlined in Lemma 1, we first formulate the SnS dual-wideband XL-MIMO channel estimation problem as a sparse signal recovery task. Subsequently, to account for the global block sparsity and local common-delay sparsity, we introduce a novel column-wise sparse prior model tailored to this structure.

A. Problem Formulation

Motivated by the sparsity of SnS dual-wideband XL-MIMO channels in the angular-delay domain, the channel estimation problem can be formulated as a multiple measurement vectors (MMV) based sparse recovery problem. Utilizing the angular-delay representation in (15), the received signal model in (3) can be further written as

$$\mathbf{Y} = \mathbf{W} \mathbf{F}_A \mathbf{X} \mathbf{F}_D + \mathbf{N} = \mathbf{\Psi} \mathbf{X} \mathbf{F}_D + \mathbf{N}, \quad (20)$$

where $\mathbf{\Psi} \triangleq \mathbf{W} \mathbf{F}_A \in \mathbb{C}^{M \times N}$. Furthermore, utilizing the unitary property of \mathbf{F}_D , (20) can be reformulated as

$$\tilde{\mathbf{Y}} = \mathbf{Y} \mathbf{F}_D^H = \mathbf{\Psi} \mathbf{X} + \tilde{\mathbf{N}}, \quad (21)$$

where $\tilde{\mathbf{Y}} = \mathbf{Y} \mathbf{F}_D^H \in \mathbb{C}^{M \times K}$ and $\tilde{\mathbf{N}} = \mathbf{N} \mathbf{F}_D^H \in \mathbb{C}^{M \times K}$ denotes the equivalent received pilot signal and noise matrix.

In this paper, our primary objective is to develop an effective estimation algorithm for accurately reconstructing \mathbf{X} or \mathbf{H}

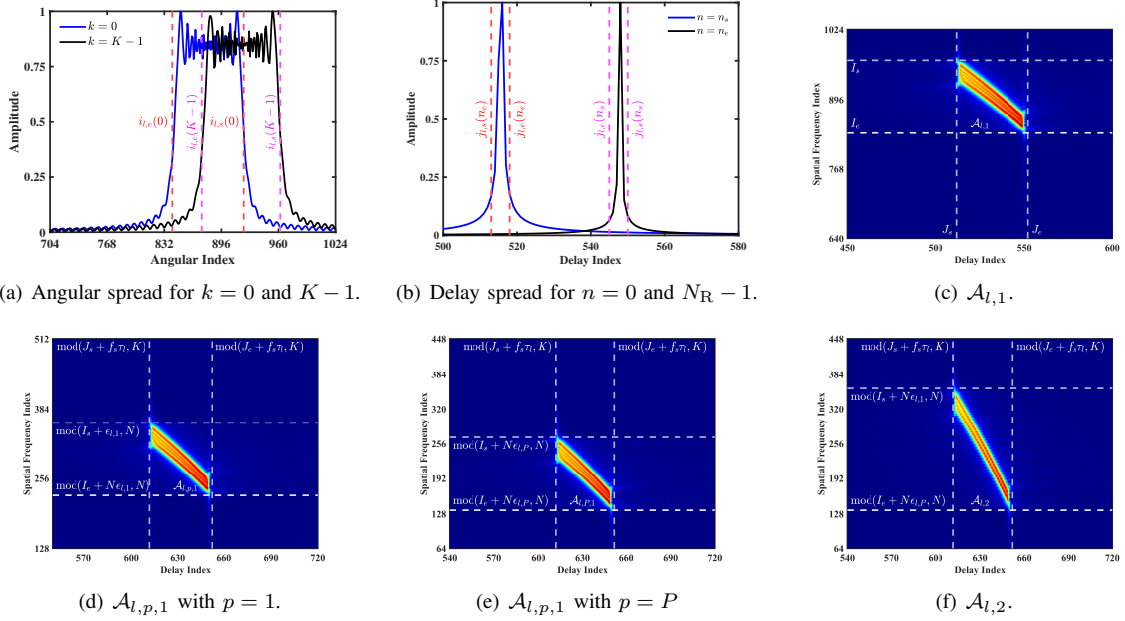


Fig. 2. Illustration of block sparsity of SnS XL-MIMO channel in the angular-delay domain.

according to \mathbf{Y} and Ψ . In the existing literature, several sparse signal recovery algorithms have been employed to address the problem in (21), including orthogonal matching pursuit (OMP) [28], [29] and optimization-based methods [30], [31]. However, these methods fail to effectively exploit the inherent sparsity structure of the angular-delay channel and often require additional parameters, such as the rank of \mathbf{X} or the number of multipaths, which may not always be available.

Considering the block sparsity of \mathbf{X} , Bayesian inference techniques such as approximate message passing (AMP) and sparse Bayesian learning (SBL) have shown superior recovery performance in channel estimation tasks [27], [32]–[34]. However, the effectiveness of these Bayesian methods relies heavily on the accuracy of the prior model. To address this, we propose a novel column-wise hierarchical sparse prior model, as detailed in the next section.

B. Column-Wise Hierarchical Sparse Prior Model

To capture the global and local common-delay sparsity characteristics of \mathbf{X} , the column-wise hierarchical prior model is characterized as

$$p(\mathbf{X}, \Gamma, \Omega, \mathbf{S}) = p(\mathbf{X}|\Gamma)p(\Gamma|\Omega, \mathbf{S})p(\Omega)p(\mathbf{S}), \quad (22)$$

where the first layer is modeled as a complex Gaussian distribution with mean zero and variance $[\Gamma]_{n,k} = \gamma_{n,k}^{-1}$, i.e.,

$$p(\mathbf{X}|\Gamma) = \prod_{n=1}^N \prod_{k=1}^K \mathcal{CN}(x_{n,k}; 0, \gamma_{n,k}^{-1}). \quad (23)$$

In the second layer, each $\gamma_{n,k}$ is assigned a conditionally Bernoulli distribution given by

$$p(\Gamma|\Omega, \mathbf{S}) = \prod_{n=1}^N \prod_{k=1}^K \delta(\gamma_{n,k} - t(s_{n,k}, \alpha_k)), \quad (24)$$

where $t(s_{n,k}, \alpha_k) = \delta(1 - s_{n,k})\alpha_k^1 + \delta(1 + s_{n,k})\alpha_k^2$ with $\alpha_k = [\alpha_k^1, \alpha_k^2]^T$ and $\delta(\cdot)$ indicating the Dirac delta function. The precision parameter $\Omega = [\alpha_1, \alpha_2, \dots, \alpha_K]^T \in \mathbb{R}^{2 \times K}$ of Γ is characterized by

$$p(\Omega) = \prod_{i=1}^2 \prod_{k=1}^K p(\alpha_k^i) = \prod_{i=1}^2 \prod_{k=1}^K \text{Ga}(\alpha_k^i; a_i, b_i), \quad (25)$$

In the third layer, to capture the global block sparsity, the variance state variable \mathbf{S} is modeled as a MRF

$$p(\mathbf{S}) = \left(\prod_{n,k} \prod_{(n',k') \in \mathcal{D}_{n,k}} u(s_{n,k}, s_{n',k'}) \right)^{\frac{1}{2}} \prod_{n,k} v(s_{n,k}), \quad (26)$$

where $\mathcal{D}_{n,k}$ denotes the element set of neighbor nodes of $s_{n,k}$ with $u(s_{n,k}, s_{n',k'}) = \exp(\varpi s_{n,k} s_{n',k'})$, and $v(s_{n,k}) = \exp(-\eta s_{n,k})$; ϖ and η are the parameters of $p(\mathbf{S})$.

In the following, we discuss how prior models in (22)–(26) capture the structured sparsity in \mathbf{X} .

- 1) Variance-Driven Sparsity:** The variance $\gamma_{n,k}^{-1}$ controls the sparsity of $x_{n,k}$, with values approaching zero effectively setting $x_{n,k}$ to zero.
- 2) Global Block Sparsity:** The MRF models the variance states, encouraging block patterns while suppressing isolated coefficients that deviate from their neighbors.
- 3) Local Common-Delay Sparsity:** As described in (24) and (25), the common-delay sparsity mechanism is introduced to ensure that, for a fixed k , all $x_{n,k}$ sharing the same variance state are governed by a common variance precision parameter. This enforces a unified sparsity structure among components associated with the same delay.

C. Bayesian Inference

Since the measurement matrix Ψ may be “bad” (e.g., rank-deficient, ill-conditioned, or having a non-zero mean) [32], the divergence issues might be arisen in the Bayesian inference. To address this, we first perform unitary transformations on

TABLE I. Factor and Distribution in (29)

Factor	Distribution	Function
f_β	$p(\beta)$	β^{-1}
$f_{r_{m,k}}$	$p(r_{m,k} z_{m,k}, \beta)$	$\mathcal{CN}(r_{m,k}; z_{m,k}, \beta^{-1})$
$f_{z_{m,k}}$	$p(z_{m,k} \mathbf{x}_k)$	$\delta(z_{m,k} - \mathbf{A}_m \cdot \mathbf{x}_k)$
$f_{x_{n,k}}$	$p(x_{n,k} \gamma_{n,k})$	$\mathcal{CN}(x_{n,k}; 0, \gamma_{n,k}^{-1})$
$f_{\gamma_{n,k}}$	$p(\gamma_{n,k} \boldsymbol{\alpha}_k, s_{n,k})$	$\delta(\gamma_{n,k} - t(s_{n,k}, \boldsymbol{\alpha}_k))$

the measurement matrix, i.e., $\Psi = \mathbf{U}\Lambda\mathbf{V}^H$. Consequently, the original signal model in (21) is rewritten as

$$\mathbf{R} = \mathbf{AX} + \mathbf{W} = \mathbf{Z} + \boldsymbol{\Xi}, \quad (27)$$

where $\mathbf{R} = \mathbf{U}^H \tilde{\mathbf{Y}}$, $\mathbf{A} = \Lambda \mathbf{V}^H$, $\mathbf{Z} = \mathbf{AX}$, and $\boldsymbol{\Xi} = \mathbf{U}^H \tilde{\mathbf{N}}$.

Based on the prior model provided in (22), the minimum mean square error (MMSE) estimator for the (n, k) -th entry of \mathbf{X} can be expressed as

$$\hat{x}_{n,k} = \int x_{n,k} p(\beta, \mathbf{Z}, \mathbf{X}, \boldsymbol{\Gamma}, \boldsymbol{\Omega}, \mathbf{S} | \mathbf{R}) d\beta d\mathbf{Z} d\boldsymbol{\Gamma} d\boldsymbol{\Omega} d\mathbf{S} d\mathbf{X}, \quad (28)$$

where $p(\beta, \mathbf{Z}, \mathbf{X}, \boldsymbol{\Gamma}, \boldsymbol{\Omega}, \mathbf{S} | \mathbf{R})$ denotes the joint posterior probability of β , \mathbf{Z} , \mathbf{X} , $\boldsymbol{\Gamma}$, $\boldsymbol{\Omega}$, and \mathbf{S} , satisfying

$$\begin{aligned} p(\beta, \mathbf{Z}, \mathbf{X}, \boldsymbol{\Gamma}, \boldsymbol{\Omega}, \mathbf{S} | \mathbf{R}) &\propto p(\beta, \mathbf{Z}, \mathbf{X}, \boldsymbol{\Gamma}, \boldsymbol{\Omega}, \mathbf{S}, \mathbf{R}) \\ &= p(\mathbf{R} | \mathbf{Z}, \beta) p(\mathbf{Z} | \mathbf{X}) p(\mathbf{X} | \boldsymbol{\Gamma}) p(\boldsymbol{\Gamma} | \boldsymbol{\Omega}, \mathbf{S}) p(\boldsymbol{\Omega}) p(\mathbf{S}) p(\beta), \end{aligned} \quad (29)$$

where $p(\beta) \propto \beta^{-1}$ denotes the noise precise level; $p(\mathbf{R} | \mathbf{Z}, \beta)$ and $p(\mathbf{Z} | \mathbf{X})$ are given by

$$p(\mathbf{R} | \mathbf{Z}, \beta) = \frac{1}{(\pi \beta^{-1})^{MK}} \prod_{m=1}^M \prod_{k=1}^K p(r_{m,k} | z_{m,k}), \quad (30)$$

$$p(\mathbf{Z} | \mathbf{X}) = \delta(\mathbf{Z} - \mathbf{AX}), \quad (31)$$

where $p(r_{m,k} | z_{m,k}) = \mathcal{CN}(r_{m,k}; z_{m,k}, \beta^{-1})$; $r_{m,k}$ and $z_{m,k}$ denote the (m, k) -th elements of \mathbf{R} and \mathbf{Z} . The dependencies of the random variables in the factorization (29) can be shown by a factor graph as depicted in Fig. 3, where the involved probability distributions are listed in Table I.

Due to the large number of antennas and subcarriers in XL-MIMO systems, solving problem (28) requires evaluating high-dimensional integrals, which is computationally prohibitive. Moreover, traditional SBL-based methods are infeasible in this context as they involve high-dimensional matrix inversions. In addition, the introduction of the common-delay sparsity mechanism and the MRF results in a more complex factor graph representation, making existing message passing algorithms [27], [32], [33], [35] less suitable. Specifically, [32], [33], [35] do not incorporate the common-delay sparsity mechanism or MRF-based variance state modeling, leading to a mismatch between these algorithms and the factor graph representation in Fig. 3. Additionally, [27] lacks the common-delay sparsity mechanism and uses a first-moment matching method to update the prior parameters, which neglects higher-order dependencies among variable nodes. To address these limitations, we propose a novel MMV-VMP algorithm utilizing the variational message passing and belief propagation in the next section.

V. PROPOSED MMV-VMP ALGORITHM

The MMV-VMP algorithm iteratively updates messages between adjacent nodes and aggregates them at the nodes $x_{n,k}$

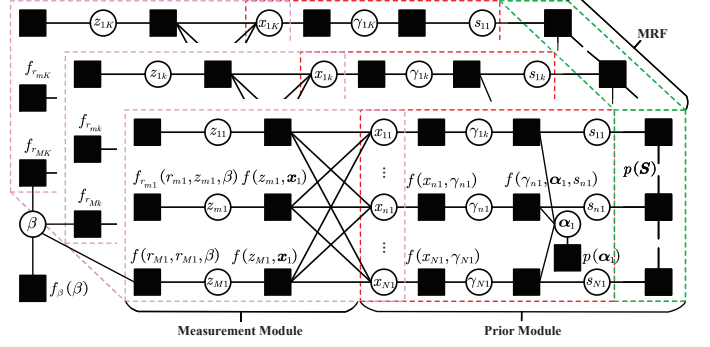


Fig. 3. Factor graph representation for the factorization (29).

to compute the corresponding posterior distributions, thereby circumventing the computationally intensive high-dimensional integrals in (28). In the following sections, we introduce the details of the forward and backward message passing in measurement and prior modules as shown in Fig. 3.

A. Measurement Module

Measurement module aims to obtain the likelihood estimation of $x_{n,k}$ based on the observation \mathbf{R} . Denote the belief of $z_{m,k}$ as $b(z_{m,k}) \sim \mathcal{CN}(z_{m,k}; \hat{z}_{m,k}, \hat{\nu}_{m,k}^z)$, which is defined in (38) with $\hat{z}_{m,k}$ and $\hat{\nu}_{m,k}^z$ indicating the m -th elements of $\hat{\mathbf{z}}_k$ and $\hat{\mathbf{\nu}}_{\mathbf{z}_k}$, respectively. In this manner, according to the variation message passing rule, the message from $f_{r_{m,k}}$ to β is given by

$$\begin{aligned} m_{f_{r_{m,k}} \rightarrow \beta} &\propto \exp \left\{ \int \ln f_{r_{m,k}} b(z_{m,k}) dz_{m,k} \right\}, \\ &\stackrel{(a)}{\propto} \beta \exp \left\{ -\beta \left(|r_{m,k} - \hat{z}_{m,k}|^2 + \hat{\nu}_{m,k}^z \right) \right\}, \end{aligned} \quad (32)$$

where (a) is obtained by utilizing the first-order and second-order moment properties of Gaussian distribution.

Concentrating all messages that are input to β , the belief of β is given by

$$\begin{aligned} b(\beta) &\propto f_\beta(\beta) \prod_{m=1}^M \prod_{k=1}^K m_{f_{r_{m,k}} \rightarrow \beta}(\beta), \\ &\propto \beta^{MK-1} \exp \left\{ -\beta \sum_{m=1}^M \sum_{k=1}^K \left(|r_{m,k} - \hat{z}_{m,k}|^2 + \hat{\nu}_{m,k}^z \right) \right\}, \end{aligned} \quad (33)$$

According to (33), it is observed that the belief $b(\beta)$ obeys the Gamma distribution with shape parameters MK and $\sum_{m=1}^M \sum_{k=1}^K (|r_{m,k} - \hat{z}_{m,k}|^2 + \hat{\nu}_{m,k}^z)$. Thus, the approximate posterior mean $\hat{\beta} = \int \beta b(\beta) d\beta$ is given by

$$\hat{\beta} = \frac{MK}{\sum_{m=1}^M \sum_{k=1}^K (|r_{m,k} - \hat{z}_{m,k}|^2 + \hat{\nu}_{m,k}^z)}. \quad (34)$$

Similar to (32), the forward message passing from $f_{r_{m,k}}$ to $z_{m,k}$ can be given by

$$\begin{aligned} m_{f_{r_{m,k}} \rightarrow z_{m,k}} &\propto \exp \left\{ \int b(\beta) \ln f_{r_{m,k}} d\beta \right\} \\ &\propto \exp \left\{ -|r_{m,k} - z_{m,k}|^2 \int \beta b(\beta) d\beta \right\} \\ &\stackrel{(a)}{\propto} \mathcal{CN}(z_{m,k}; r_{m,k}, \hat{\beta}^{-1}), \end{aligned} \quad (35)$$

where (a) is obtained by utilizing (34). Owing to the Gaussian form of the message in (35), we can obtain the following model $\mathbf{r}_k = \mathbf{z}_k + \boldsymbol{\xi}_k$, where $\boldsymbol{\xi}_k \sim \mathcal{CN}(\boldsymbol{\xi}_k; 0, \hat{\beta}^{-1} \mathbf{I}_{M \times M})$. This representation facilitates seamless integration with the forward passing of UAMP in the measurement module.

Denote the posterior mean and variance of \mathbf{x}_k as $\hat{\mathbf{x}}_k$ and $\hat{\nu}_{\mathbf{x}_k}$, which is defined in (55) and (56). According to the UAMP rules [33], define $\boldsymbol{\lambda}$ as $|\mathbf{A}|^2 \mathbf{1}_N$. Thus, the message from \mathbf{z}_k to $f_{\mathbf{r}_k}$ is given by $\mathcal{CN}(\mathbf{z}_k; \mathbf{p}_k, \boldsymbol{\nu}_{\mathbf{p}_k})$ with

$$\boldsymbol{\nu}_{\mathbf{p}_k} = \boldsymbol{\lambda} \hat{\nu}_{\mathbf{x}_k}, \quad \mathbf{p}_k = \mathbf{A} \hat{\mathbf{x}}_k - \boldsymbol{\nu}_{\mathbf{p}_k} \odot \boldsymbol{\mu}_k, \quad (36)$$

where \odot denotes the element product; $\boldsymbol{\mu}_k$ is a intermediate vector, which is updated by

$$\boldsymbol{\nu}_{\boldsymbol{\mu}_k} = \mathbf{1}_M \cdot (1_M \hat{\beta}^{-1} + \boldsymbol{\nu}_{\mathbf{p}_k}), \quad \boldsymbol{\mu}_k = \boldsymbol{\nu}_{\boldsymbol{\mu}_k} \odot (\mathbf{r}_k - \mathbf{p}_k). \quad (37)$$

In this case, utilizing the sum-product rule, the belief of \mathbf{z}_k is given by

$$\begin{aligned} b(\mathbf{z}_k) &= \mathcal{CN}(\mathbf{z}_k; \mathbf{p}_k, \boldsymbol{\nu}_{\mathbf{p}_k}) \prod_{m=1} m_{f_{\mathbf{r}_{m,k}} \rightarrow z_{m,k}}(z_{m,k}) \\ &= \mathcal{CN}(\mathbf{z}_k; \mathbf{p}_k, \boldsymbol{\nu}_{\mathbf{p}_k}) \mathcal{CN}(\mathbf{z}_k; \mathbf{r}_k, \hat{\beta}^{-1} \mathbf{I}_{M \times M}) \\ &\stackrel{(a)}{\propto} \mathcal{CN}(\mathbf{z}_k; \hat{\mathbf{z}}_k, \boldsymbol{\nu}_{\mathbf{z}_k}), \end{aligned} \quad (38)$$

where (a) is obtained by the property of Gaussian distribution, i.e., $\mathcal{CN}(x; \mu_1, \nu_1) \mathcal{CN}(x; \mu_2, \nu_2) \propto \mathcal{CN}(x; \mu, \nu)$ with $\nu = (1/\nu_1 + 1/\nu_2)^{-1}$ and $\mu = \nu(\mu_1/\nu_1 + \mu_2/\nu_2)$; In addition, $\boldsymbol{\mu}_k$ and $\boldsymbol{\nu}_{\boldsymbol{\mu}_k}$ are respectively given by

$$\boldsymbol{\nu}_{\mathbf{z}_k} = \boldsymbol{\nu}_{\mathbf{p}_k} \cdot (1 + \hat{\beta} \boldsymbol{\nu}_{\mathbf{p}_k}), \quad (39)$$

$$\hat{\mathbf{z}}_k = (\mathbf{p}_k + \hat{\beta} \boldsymbol{\nu}_{\mathbf{p}_k} \odot \mathbf{r}_k) \cdot (1 + \hat{\beta} \boldsymbol{\nu}_{\mathbf{p}_k}). \quad (40)$$

Moreover, the output message from measurement module is given by

$$\boldsymbol{\nu}_{\mathbf{q}_k} = \mathbf{1} \cdot (|\mathbf{A}|^2 \boldsymbol{\nu}_{\boldsymbol{\mu}_k}), \quad \mathbf{q}_k = \hat{\mathbf{x}}_k + \boldsymbol{\nu}_{\mathbf{q}_k} \odot (\mathbf{A}^H \boldsymbol{\mu}_k). \quad (41)$$

B. Sparse Prior Module

The aim of the prior module is to update the distribution of $x_{n,k}$ according to extrinsic message $m_{x_{n,k} \rightarrow f_{x_{n,k}}}(x_{n,k}) \propto \mathcal{CN}(x_{n,k}; q_{n,k}, \nu_{n,k}^q)$ and calculate the posterior estimation $\hat{x}_{n,k}$ and $\hat{\nu}_{\mathbf{x}_k}$, where $q_{n,k}$ and $\nu_{n,k}^q$ denotes the n -th element of \mathbf{q}_k and $\boldsymbol{\nu}_{\mathbf{q}_k}$, respectively.

1) *Forward Message Passing*: Denote the belief of $x_{n,k}$ as $b(x_{n,k}; \hat{x}_{n,k}, \hat{\nu}_{\mathbf{x}_k})$, defined in (54). Utilizing the variational message passing rule, similar to (32), the message from $f_{x_{n,k}}$ to $\gamma_{n,k}$ is given by

$$\begin{aligned} m_{f_{x_{n,k}} \rightarrow \gamma_{n,k}} &\propto \exp \left\{ \int b(x_{n,k}) \ln f_{x_{n,k}} dx_{n,k} \right\} \\ &\propto \gamma_{n,k} \exp(-\gamma_{n,k} (|\hat{x}_{n,k}|^2 + \hat{\nu}_{\mathbf{x}_k})). \end{aligned} \quad (42)$$

Further, according to sum-product rule, the message from $f_{\gamma_{n,k}}$ to $s_{n,k}$ is given by

$$\begin{aligned} m_{f_{\gamma_{n,k}} \rightarrow s_{n,k}} &\stackrel{(a)}{\propto} \int f_{\gamma_{n,k}} m_{f_{x_{n,k}} \rightarrow \gamma_{n,k}} b(\boldsymbol{\alpha}_k) d\gamma_{n,k} d\boldsymbol{\alpha}_k \\ &= \pi_{n,k}^{\text{out}} \delta(1 - s_{n,k}) + (1 - \pi_{n,k}^{\text{out}}) \delta(1 + s_{n,k}), \end{aligned} \quad (43)$$

where (a) is obtained by utilizing the approximation $b(\boldsymbol{\alpha}_k) = b(\alpha_k^1) b(\alpha_k^2) \approx \prod_{j \neq n} m_{\boldsymbol{\alpha}_k \rightarrow f_{\gamma_{j,k}}}$ and the expectation of Gamma distribution; π_n^{out} is defined as

$$\pi_{n,k}^{\text{out}} = \frac{\hat{a}_k^1 (\hat{b}_k^2 + |\hat{x}_{n,k}|^2 + \hat{\nu}_{\mathbf{x}_k})}{\hat{a}_k^1 (\hat{b}_k^2 + |\hat{x}_{n,k}|^2 + \hat{\nu}_{\mathbf{x}_k}) + \hat{a}_k^2 (\hat{b}_k^1 + |\hat{x}_{n,k}|^2 + \hat{\nu}_{\mathbf{x}_k})}.$$

Utilizing the message $m_{f_{\gamma_{n,k}} \rightarrow s_{n,k}}(s_{n,k})$, we further derive the message update in the MRF with a 4-connect scheme, where $s_{n,k}^l \triangleq s_{n,k-1}$, $s_{n,k}^r \triangleq s_{n,k+1}$, $s_{n,k}^t \triangleq s_{n-1,k}$, and $s_{n,k}^b \triangleq s_{n,k+1}$ denote the left, right, top and bottom neighbors of $x_{n,k}$. The input message of $s_{n,k}$ from left, right, top and bottom neighbors, denoted as $m_{n,k}^l$, $m_{n,k}^r$, $m_{n,k}^t$, and $m_{n,k}^b$, are Bernoulli distributions. Take $m_{n,k}^l$ as an example, according to the sum-product rule, we have $m_{n,k}^l \propto \lambda_{n,k}^l \delta(1 - s_{n,k}) + (1 - \lambda_{n,k}^l) \delta(1 + s_{n,k})$, where $\lambda_{n,k}^l$ is given by (45), as shown in the top of next page. The other three messages can be obtained in a similar way.

2) *Backward Message Passing*: With the messages of neighbors and $v(s_{n,k})$, the message from $s_{n,k}$ to $f_{\gamma_{n,k}}$ can be given by

$$\begin{aligned} m_{s_{n,k} \rightarrow f_{\gamma_{n,k}}} &= \prod_{w \in \{l, r, t, b\}} m_{n,k}^w v(s_{n,k}) \\ &\propto \pi_{n,k}^{\text{in}} \delta(1 - s_{n,k}) + (1 - \pi_{n,k}^{\text{in}}) \delta(1 + s_{n,k}) \end{aligned} \quad (46)$$

where $\pi_{n,k}^{\text{in}}$ is defined as

$$\frac{e^{-\eta} \prod_{w \in \{l, r, t, b\}} \lambda_{n,k}^w}{e^{-\eta} \prod_{w \in \{l, r, t, b\}} \lambda_{n,k}^w + e^{\eta} \prod_{w \in \{l, r, t, b\}} (1 - \lambda_{n,k}^w)}. \quad (47)$$

According to sum-product rule, the message from $f_{\gamma_{n,k}}$ to α_k^1 is given by

$$\begin{aligned} m_{f_{\gamma_{n,k}} \rightarrow \alpha_k^1} &\propto \int f_{\gamma_{n,k}} m_{f_{x_{n,k}} \rightarrow \gamma_{n,k}} m_{s_{n,k} \rightarrow f_{\gamma_{n,k}}} d\gamma_{n,k} ds_{n,k}, \\ &\stackrel{(a)}{\propto} \alpha_k^1 \exp(-\alpha_k^1 (|\hat{x}_{n,k}|^2 + \hat{\nu}_{\mathbf{x}_k})), \end{aligned} \quad (48)$$

where (a) is obtained by utilizing the property of delta function, i.e., $\int \delta(x - t) f(x) dx = f(t)$. Similarly, $m_{f_{\gamma_{n,k}} \rightarrow \alpha_k^2} \propto \alpha_k^2 \exp(-\alpha_k^2 (|\hat{x}_{n,k}|^2 + \hat{\nu}_{\mathbf{x}_k}))$. As a result, the belief of α_k^1 is given by

$$b(\alpha_k^1) \propto p(\alpha_k^1) \prod_n m_{f_{\gamma_{n,k}} \rightarrow \alpha_k^1}(\alpha_k^1) \propto \text{Ga}(\alpha_k^1; \hat{a}_k^1, \hat{b}_k^1), \quad (49)$$

where $\hat{a}_k^1 = a_1 + N$ and $\hat{b}_k^1 = b_1 + \sum_{n=1}^N |\hat{x}_{n,k}|^2 + \hat{\nu}_{\mathbf{x}_k}$. Similarly, we have $b(\alpha_k^2) \propto \text{Ga}(\alpha_k^2; \hat{a}_k^2, \hat{b}_k^2)$ with $\hat{a}_k^2 = a_2 + N$ and $\hat{b}_k^2 = b_2 + \sum_{n=1}^N |\hat{x}_{n,k}|^2 + \hat{\nu}_{\mathbf{x}_k}$. According to the sum-product rule, the message from $f_{\gamma_{n,k}}$ to $\gamma_{n,k}$ is given by

$$m_{f_{\gamma_{n,k}} \rightarrow \gamma_{n,k}} = \pi_{n,j}^{\text{in}} b(\alpha_k^1) + (1 - \pi_{n,j}^{\text{in}}) b(\alpha_k^2). \quad (50)$$

Consequently, the belief of $\gamma_{n,k}$ is given by

$$\begin{aligned} b(\gamma_{n,k}) &\propto m_{f_{\gamma_{n,k}} \rightarrow \gamma_{n,k}} m_{f_{x_{n,k}} \rightarrow \gamma_{n,k}}(\gamma_{n,k}) \\ &\propto \pi_{n,j}^{\text{in}} \gamma_{n,k}^{\hat{a}_k^1} \exp(-\gamma_{n,k} (\hat{b}_k^1 + |\hat{x}_{n,k}|^2 + \hat{\nu}_{\mathbf{x}_k})) \\ &\quad + (1 - \pi_{n,k}^{\text{in}}) \gamma_{n,k}^{\hat{a}_k^2} \exp(-\gamma_{n,k} (\hat{b}_k^2 + |\hat{x}_{n,k}|^2 + \hat{\nu}_{\mathbf{x}_k})). \end{aligned} \quad (51)$$

$$\lambda_{n,j}^1 = \frac{\pi_{s_{n,j}^l}^{\text{out}} e^{\varpi - \eta} \prod_{w \in \{l, t, b\}} \lambda_{s_{n,j}^l}^w + (1 - \pi_{s_{n,j}^l}^{\text{out}}) e^{\eta - \varpi} \prod_{w \in \{l, t, b\}} (1 - \lambda_{s_{n,j}^l}^w)}{(e^{\varpi} + e^{-\varpi}) \left(e^{-\eta} \pi_{s_{n,j}^l}^{\text{out}} \prod_{w \in \{l, t, b\}} \lambda_{s_{n,j}^l}^w + e^{\eta} (1 - \pi_{s_{n,j}^l}^{\text{out}}) \prod_{w \in \{l, t, b\}} (1 - \lambda_{s_{n,j}^l}^w) \right)}. \quad (45)$$

As a result, the message from $f_{x_{n,k}}$ to $x_{n,k}$ is denoted as

$$\begin{aligned} m_{f_{x_{n,k}} \rightarrow x_{n,k}}(x_{n,k}) &\propto \exp \left\{ \int b(\gamma_{n,k}) \ln f_{x_{n,k}} d\gamma_{n,k} \right\} \\ &\propto \exp \left\{ - \int |x_{n,k}|^2 \gamma_{n,k} b(\gamma_{n,k}) d\gamma_{n,k} \right\} \\ &\stackrel{(a)}{\propto} \mathcal{CN}(x_{n,k}; 0, \hat{\gamma}_{n,k}^{-1}), \end{aligned} \quad (52)$$

where (a) is obtained by

$$\begin{aligned} \hat{\gamma}_{n,j} &= \int \gamma_{n,k} b(\gamma_{n,k}) d\gamma_{n,k} = \pi_{n,k}^{\text{in}} \frac{\hat{a}_k^1 + 1}{\hat{b}_k^1 + |\hat{x}_{n,k}|^2 + \hat{\nu}_{\mathbf{x}_k}} \\ &\quad + (1 - \pi_{n,k}^{\text{in}}) \frac{\hat{a}_k^2 + 1}{\hat{b}_k^2 + |\hat{x}_{n,k}|^2 + \hat{\nu}_{\mathbf{x}_k}}. \end{aligned} \quad (53)$$

Combining the message from measurement module as $\mathcal{CN}(x_{n,k}; q_{n,k}, \nu_{n,k}^q)$. Thus, the approximate posterior distribution of $x_{n,j}$ can be approximated as

$$\begin{aligned} b(x_{n,k}) &\propto \mathcal{CN}(x_{n,k}; q_{n,k}, \nu_{n,k}^q) \mathcal{CN}(x_{n,k}; 0, \hat{\gamma}_{n,k}^{-1}) \\ &\stackrel{(a)}{\propto} \mathcal{CN}(x_{n,k}; \hat{x}_{n,k}, \hat{\nu}_{\mathbf{x}_k}), \end{aligned} \quad (54)$$

where (a) is obtained similar to (38), and the approximate posterior mean and variance of $x_{n,k}$ are respectively given by

$$\hat{\nu}_{n,k}^x = \frac{\nu_{n,k}^q}{1 + \nu_{n,k}^q \hat{\gamma}_{n,k}}, \quad \hat{x}_{n,k} = \frac{q_{n,k}}{1 + \nu_{n,k}^q \hat{\gamma}_{n,k}}. \quad (55)$$

Performing the average operations to $\nu_{n,k}^x$, we further have

$$\hat{\nu}_{\mathbf{x}_k} = \frac{1}{N} \sum_{n=1}^N \hat{\nu}_{n,k}^x. \quad (56)$$

The proposed MMV-VMP algorithm is summarized in Algorithm 1 and it can be terminated when it reached a maximum number of iteration or the difference between the estimates of two consecutive iterations is less than 10^{-5} . In the following, we provide the computational complexity analysis for the proposed MMV-VMP algorithm. Examining the steps of Algorithm 1, it is evident that there is no matrix inversion involved. Thus, the most computationally intensive parts only involve matrix-vector products in lines 2 and 6, i.e., $\mathcal{O}(MN)$ per iteration. Consequently, the total complexity of the MMV-VMP algorithm is $\mathcal{O}(TKMN)$, where T denotes the number of iterations.

VI. SIMULATION RESULTS

In this section, we evaluate the performance of the proposed channel estimation scheme under various system setups. The simulation parameters are shown in Table II. In particular, we consider normalized mean square error (NMSE) as performance metrics, which is defined as $\text{NMSE} \triangleq \|\hat{\mathbf{H}} - \mathbf{H}\|_{\text{F}}^2 / \|\mathbf{H}\|_{\text{F}}^2$, where \mathbf{H} and $\hat{\mathbf{H}}$ are the true channel and estimated channel, respectively. In addition, the SNR is defined

Algorithm 1 Proposed UAMP-SBL-MRF algorithm

Input: received vector \mathbf{R} , measurement matrix \mathbf{A} .

Initialize: $\hat{\nu}_{\mathbf{x}_k}^{(0)} = 1$, $\hat{\mathbf{x}} = \mathbf{0}$, $\hat{\gamma}_{n,k} = 1$, $\hat{\beta} = 1$, and $\boldsymbol{\mu} = \mathbf{0}$.

1: **while** the stopping criterion is not met **do**

 /***Measurement module***/

 2: Update the $\boldsymbol{\nu}_{\mathbf{p}_k}$ and \mathbf{p}_k according to (36);

 3: Update the $\boldsymbol{\nu}_{\boldsymbol{\mu}_k}$ and $\boldsymbol{\mu}_k$ according to (37);

 4: Update the $\boldsymbol{\nu}_{\mathbf{z}_k}$ and \mathbf{z}_k according to (39) and (40);

 5: Update $\hat{\beta}$ according to (34);

 6: Update the $\boldsymbol{\nu}_{\mathbf{q}_k}$ and \mathbf{q}_k according to (41);

 /***Prior Module***/

 7: Update the messages $m_{f_{x_{n,k}} \rightarrow \gamma_{n,k}}$ according to (43);

 8: Update the messages m_n^l, m_n^r, m_n^t , and m_n^b ;

 9: Update the messages $m_{s_n \rightarrow f_{\gamma_n}}(s_n)$ according to (47);

 10: Update the belief $b(\alpha_k^1)$ and $b(\alpha_k^2)$ according to (49);

 11: Update $\hat{\gamma}_n$ according to (53);

 12: Update $\hat{x}_{n,k}$ and $\hat{\nu}_{\mathbf{x}_k}$ according to (55) and (56).

13: **end while**

Output: $\hat{x}_{n,k}$.

TABLE II. Simulation Parameters

Notations	Parameters
Number of BS antenna N_R	256
Number of RF chain N_{RF}	16
Carrier frequency f_c	30GHz
Number of pilot carriers K	64
System bandwidth f_s	1.6GHz
Number of channel path L	4
Angle of arrival ϑ_l	$\mathcal{U}(-\pi/2, \pi/2)$
Distance between BS and UE or scatterers r_l	[5, 50]m
Proportion of visible antenna elements ρ_l	(0, 1]

in received side, which is given by $10 \log_{10} (\|\mathbf{W}\mathbf{H}\|_{\text{F}}^2 / \|\mathbf{N}\|_{\text{F}}^2)$. Additionally, we compare the proposed MMV-VMP algorithm with the following baselines:

- **SOMP** [28]: The simultaneous OMP algorithm designed for on-grid sparse recovery, which depends on the knowledge of the number of non-zeros components.
- **StdSBL** [36]: The standard SBL algorithm, implemented within an expectation-maximization (EM) framework. The algorithm employs a two-layer Gaussian-Gamma hierarchical prior model, where the posterior estimates of \mathbf{x}_k are updated in the E-step, and the hyperparameters of the prior model are updated in the M-step.
- **UAMP-SBL** [33]: An improved version of the StdSBL algorithm that leverages the unitary AMP framework to perform the E-step and variational message passing to achieve the updates of prior parameters.
- **PC-SBL** [37]: A variant of the StdSBL framework that incorporates a pattern-coupled Gaussian prior model to exploit the block sparsity inherent in signals.
- **VSP** [27]: A variant of the StdSBL framework that em-

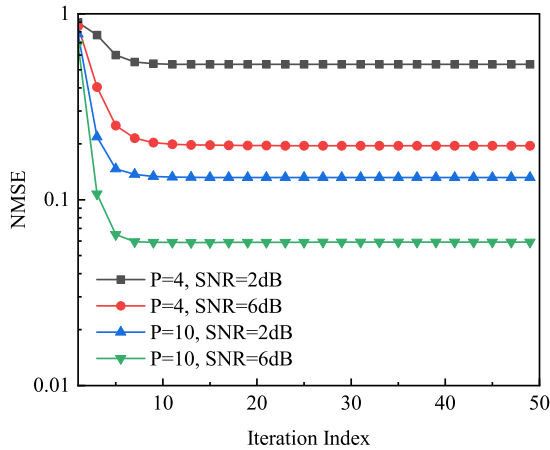


Fig. 4. Convergence behavior of MMV-VMP.

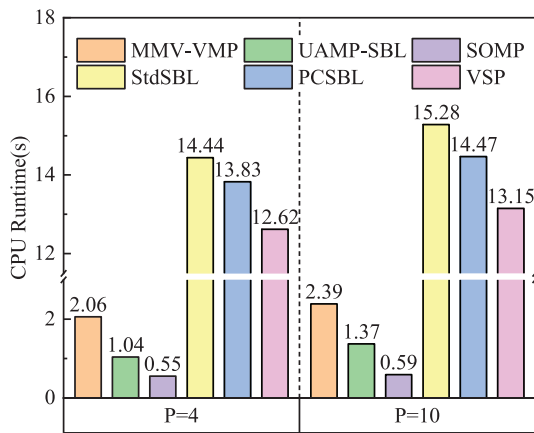


Fig. 5. Complexity evaluation of different algorithms.

loys a MRF-based hierarchical prior model to effectively capture the block sparsity of signals. Unlike the StdSBL and PC-SBL methods, the prior parameters in the VSP algorithm are updated using a moment-matching approach, providing a computationally efficient alternative.

A. Convergence and Complexity Performance

Fig. 4 illustrates the convergence behavior of the proposed MMV-VMP algorithm by plotting the NMSE against the number of iterations under various pilot lengths and SNR conditions. The results clearly demonstrate a consistent monotonic decrease in NMSE across all iterations, indicating the algorithm's stable and reliable convergence across different simulation scenarios. Based on the trade-off between estimation accuracy and computational complexity, it is observed that the NMSE stabilizes after approximately 20 iterations. Therefore, for subsequent simulations, the maximum number of iterations can be effectively limited to 20 without compromising performance.

Fig. 5 presents a computational complexity analysis by comparing the CPU runtime of various algorithms. Among these, SOMP exhibits the shortest runtime. This efficiency is attributed to its computational simplicity, involving only matrix-vector product between the residual and the measurement matrix, as well as a projection operation between the received signal and the low-dimensional basis matrix. In contrast, SBL-based methods such as StdSBL, PC-SBL, and

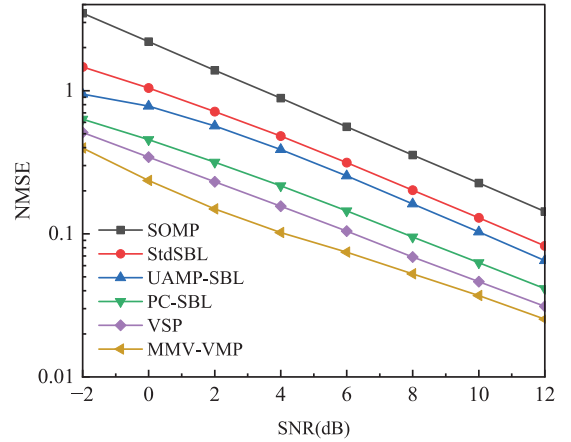


Fig. 6. NMSE versus pilot symbol number.

VSP require significantly more computational time. This is primarily due to the matrix inversion operations inherent in their implementation, which increase computational complexity. In contrast, the proposed MMV-VMP algorithm demonstrates a shorter runtime compared to StdSBL, PC-SBL, and VSP due to avoidance of matrix inversion operations and stable convergence properties.

B. NMSE versus SNR and Pilot Symbol Number

Fig. 6 illustrates the NMSE performance of various algorithms as a function of SNR for $P = 8$. The results reveal that algorithms such as SOMP [29], StdSBL [36], and UAMP-SBL [33], which fail to account for both global block sparsity and local common-delay sparsity, exhibit significantly poorer NMSE performance compared to algorithms like PC-SBL, VSP, and the proposed MMV-VMP. Among block-sparsity prior-based methods, the PC-SBL algorithm leverages a pattern-coupled Gaussian prior model to effectively capture local common-delay sparsity. However, it does not consider global block sparsity. In contrast, the VSP algorithm employs a MRF-based prior to model global block sparsity but lacks the ability to incorporate local common-delay sparsity. The proposed MMV-VMP algorithm overcomes these limitations by utilizing a tailored column-wise hierarchical prior that simultaneously incorporates both global block sparsity and local common-delay sparsity. This comprehensive modeling approach ensures consistently superior NMSE performance across the entire SNR range under consideration.

Fig. 7 evaluates the estimation performance of various algorithms under different compression ratios by varying the number of pilot symbols, P , with the fixed SNR of 2 dB. As the number of pilot symbols varies from 6 to 12, the compression ratio M/N ranges from 0.375 to 0.75. We can obtain two key observations: 1) Across most compression ratios, the proposed MMV-VMP algorithm outperforms baseline methods. This result highlights its robust sparse recovery capability under varying compression conditions. Moreover, the superior performance demonstrates that the proposed algorithm is a low-overhead solution, requiring fewer pilot symbols to achieve comparable or better performance than other algorithms. 2) As the pilot length increases, the rate of performance improvement gradually diminishes, eventually

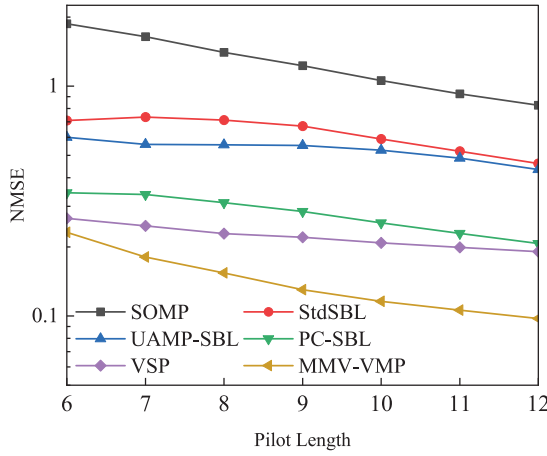


Fig. 7. NMSE versus pilot symbol number.

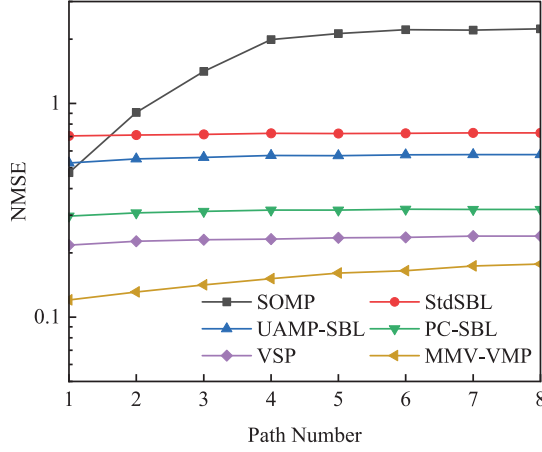


Fig. 8. NMSE versus path number.

approaching saturation. This observation suggests that selecting a moderate value of P is sufficient to strike a balance between estimation performance and pilot overhead.

C. NMSE versus Path Number

Fig. 8 illustrates the NMSE performance of various algorithms as a function of the number of propagation paths, with $P = 8$ and SNR = 2dB. The SOMP algorithm exhibits significant sensitivity to prior knowledge of the number of paths, with its performance degrading sharply when the assumed and actual path numbers differ. In contrast, Bayesian inference-based methods, leveraging sparsity-promoting prior models, adapt effectively to variations in the number of paths, maintaining consistent and robust performance across all scenarios. Notably, the proposed MMV-VMP algorithm consistently outperforms other Bayesian methods, demonstrating superior capability in handling dynamic sparse scattering environments.

D. Ablation Study to Evaluate the Effects of Prior Models

To evaluate the effectiveness of the proposed column-wise prior model, the MMV-VMP algorithm is compared with two baselines: (1) a column-wise hierarchical prior without the MRF, labeled as “Column-Wise w.o. MRF,” and (2) a column-wise prior without the common-delay sparsity mechanism, labeled as “Column-Wise w.o. CD.” Fig. 9 reveals two key observations: 1) Both the MRF and the common-delay sparsity

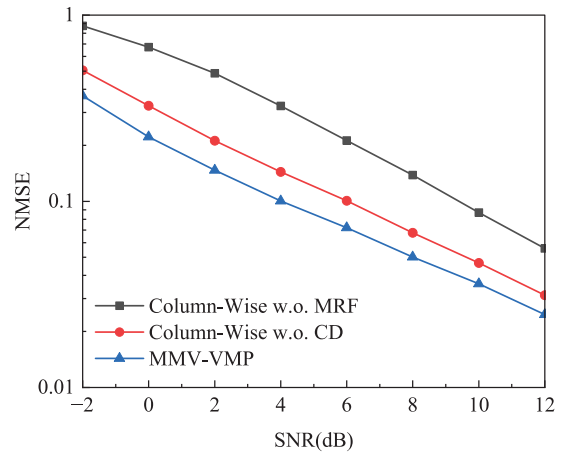


Fig. 9. Ablation study of the column-wise hierarchical model.

mechanism contribute to improved estimation performance. Notably, the improvement introduced by the MRF is more significant than that of the common-delay sparsity mechanism. 2) The simultaneous use of the MRF and the common-delay sparsity mechanism better captures the structured sparsity of the channel, leading to further enhancement in estimation accuracy.

To showcase the estimation performance of different prior more intuitively, Fig. 10 provides the results of a Monte Carlo simulation with SNR = 2 dB and $P = 8$. The original spatial-delay channels are compared with the reconstructed channels obtained using “Column-Wise w.o. MRF,” “Column-Wise w.o. CD,” and the proposed MMV-VMP algorithm. The figure clearly shows that the proposed MMV-VMP algorithm achieves the best visual quality, accurately reconstructing the spatial-delay channels and demonstrating its superior capability in sparse recovery. As expected, “Column-Wise w.o. MRF” provides the poorest reconstruction quality due to its limited ability to capture global block sparsity. Moreover, compared to “Column-Wise w.o. CD,” the reconstructed channels by MMV-VMP exhibit reduced power dispersion phenomenon near the non-zero regions, attributed to the incorporation of the common-delay sparsity mechanism.

VII. CONCLUSIONS

In this paper, we have addressed the channel estimation problem in XL-MIMO systems, taking into account the spherical wavefront effects, spatially non-stationary (SnS) properties, and dual-wideband effects. We first rigorously quantified the angular and delay spread effects of the SnS dual-wideband XL-MIMO channel in the angular-delay domain. Building upon this, we highlighted the global and local common-delay sparsity inherent in the angular-delay channels. Leveraging this structured sparsity, we proposed a computationally efficient MMV-VMP algorithm, where variational message passing is employed to handle the complex factor graph arising from the column-wise hierarchical prior. Simulation results demonstrate that the proposed MMV-VMP algorithm consistently outperforms existing methods, offering robust performance with moderate computational complexity. Additionally, an ablation study was conducted to assess the effectiveness of the column-wise hierarchical prior, further validating the advantages of the proposed approach.

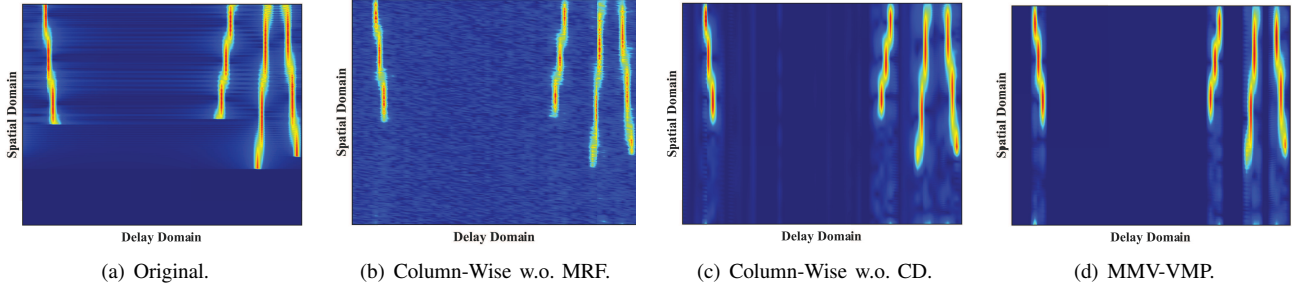


Fig. 10. Original and reconstructed channels by ‘‘Column-Wise w.o. MRF,’’ ‘‘Column-Wise w.o. CD,’’ and MMV-VMP algorithm.

APPENDIX A PROOF OF LEMMA 1

The proof of Theorem 1 is portioned as two part. We first prove that the angular-delay matrix of $\Theta(\varphi_l, \psi_l)$ is block-sparse. Then, applying the shift property of 2D-IDFT, the block sparsity of $\mathbf{X} = \mathbf{F}_A^H \mathbf{H} \mathbf{F}_D$ can be obtained. For notation simplification, we discard the subscript l , φ_l , and ψ_l in the subsequent derivations. We begin by examining the angular-domain transformation of Θ with $\cos \vartheta > 0$. Mathematically, Θ can be rewritten in a chirp signal form as

$$[\Theta]_{n,k} = e^{-j2\pi(a_k n - \frac{b_k}{2} n^2)}, \quad (\text{A.1})$$

where $a_k = f_k \psi / f_c$ and $b_k = 2f_k \varphi / f_c$ denote the starting spatial frequency and chirp rate, respectively. Utilizing the inherent chirp properties of Eq. (A.1), the IDFT of Θ for the fixed k , i.e., $[\Xi_A]_{:,k} = \mathbf{F}_A^H \theta(f_k) \in \mathbb{C}^{N \times 1}$ exhibits a distinct rectangular shape [38], where \mathbf{F}_A denotes a N -dimension DFT matrix. The boundary spatial frequencies are given by

$$i_s(k) = (a_k - b_k n_s) \lambda_c / d, \quad (\text{A.2})$$

$$i_e(k) = (a_k - b_k n_e) \lambda_c / d, \quad (\text{A.3})$$

where n_s and n_e denote the start and ending index of VR ϕ , i.e., $\phi \in [n_s, n_e]$. In this case, due to $a_k > 0$ and $b_k > 0$, we have $i_s(k) > i_e(k)$. Consequently, $[\Xi_A]_{:,k}$ demonstrates block sparsity, with its prominent spatial frequency components concentrated from $i_e(k)$ to $i_s(k)$.

Extending this observation across all K subcarriers, the overall spatial frequency range of significant components spans from $i_e^{\min} = \min_k i_e(k)$ to $i_s^{\max} = \max_k i_s(k)$. As a result, Ξ_A is characterized as a row-wise block matrix

$$\Xi_A = \left[\mathbf{0}_{K \times (I_e-1)}^T, \mathbf{U}_{K \times (I_s-I_e+1)}^T, \mathbf{0}_{K \times (N-I_s)}^T \right]^T, \quad (\text{A.4})$$

where \mathbf{U} is a non-zero matrix; index I_e and I_s are given by $I_e = \lceil (i_e^{\min} + 1)N/2 \rceil$ and $I_s = \lceil (i_s^{\max} + 1)N/2 \rceil$.

Further, we examine the IDFT of Θ in the delay domain, i.e., $\Xi_D = \Theta \mathbf{F}_D^*$, where \mathbf{F}_D denote a K -dimension DFT matrix. Specifically, we have

$$\begin{aligned} [\Xi_D]_{n,m} &\propto \frac{1}{\sqrt{K}} \sum_{k=0}^{K-1} e^{j\frac{2\pi}{K}mk} e^{-j2\pi k t_n} \\ &\propto \frac{1}{\sqrt{K}} \frac{\sin(\pi K(t_n - \frac{m}{K}))}{\sin(\pi(t_n - \frac{m}{K}))}, \end{aligned} \quad (\text{A.5})$$

where $t_n = n \frac{f_s \psi}{K f_c} - n^2 \frac{f_s \varphi}{K f_c}$, which is a quadratic function about n . Further, we have

$$\lim_{K \rightarrow \infty} |[\Xi_D]_{n,m}| \propto \sqrt{K} \delta \left(t_n - \frac{m}{K} \right). \quad (\text{A.6})$$

From (A.6), when $K \rightarrow \infty$, $[\Xi_D]_{n,:}$ can be approximated as a delta function centered at $m = t_n K$. However, due to the finite sampling size K in practice, we consider the range from $j_e(n) = (t_n - 2/K)K$ to $j_s(n) = (t_n + 2/K)K$ to collect the delay indices near the peak effectively. Extending this observation across all N antennas, Ξ_D is characterized as a column-wise block matrix

$$\Xi_D = [\mathbf{0}_{N \times (J_e-1)}, \mathbf{L}_{N \times (J_s-J_e+1)}, \mathbf{0}_{N \times (K-J_s)}], \quad (\text{A.7})$$

where $J_e = \min_n j_e(n)$ to $J_s = \max_n j_s(n)$ with $n \in \phi$, and \mathbf{L} is a non-zero matrix.

According to row-wise and column-wise block sparsity of (A.4) and (A.7), we assert that $\Xi = \mathbf{F}_A^H \Theta \mathbf{F}_D^*$ adheres to the following block-sparse structure, with its significant entries localized within the square region $\mathcal{A}_1 \triangleq \{(n, k) \in \mathbb{Z}^2 \mid I_e \leq n \leq I_s, J_e \leq k \leq J_s\}$, i.e.,

$$\Xi = \begin{bmatrix} \mathbf{0} & & & & \mathbf{0} & & & & \mathbf{0} \\ \mathbf{0} & \mathbf{V}_{(I_s-I_e+1) \times (J_s-J_e+1)} & & & \mathbf{0} & & & & \mathbf{0} \\ \mathbf{0} & & \mathbf{0} & & & & & & \mathbf{0} \end{bmatrix}, \quad (\text{A.8})$$

where \mathbf{V} denotes a non-zero matrix.

Next, we examine the 2D-IDFT of channel \mathbf{H} , $\mathbf{X} = \mathbf{F}_A^H \mathbf{H} \mathbf{F}_D^*$. By leveraging the linearity of the 2D-IDFT, we can focus solely on analyzing the l -th path. Define $\mathbf{H}_l = \alpha_l (\boldsymbol{\kappa}_l \odot \mathbf{b}(\psi_l, \varphi_l)) \mathbf{a}^T(\tau_l) \odot \Theta$, whose (n, k) -th element is given by

$$\begin{aligned} [\mathbf{H}_l]_{n,k} &\propto e^{-j2\pi(n\psi_l - n^2\varphi_l + f_k\tau_l)} [\Theta]_{n,k}, \\ &\stackrel{(a)}{\propto} \sum_{p=1}^P e^{-j2\pi(\frac{n}{N}N\epsilon_{l,p} + \frac{k}{K}f_s\tau_l)} [\Theta]_{n,k}, \end{aligned} \quad (\text{A.9})$$

where (a) is obtained by decomposing the chirp signal $e^{-j2\pi(n\psi_l - n^2\varphi_l)}$ into the superposition of P complex exponential signals with frequencies $\epsilon_{l,p} = \psi_l - 2n_{l,e}\varphi_l + \eta_l(p-1)$ with $\eta_l = 2N\varphi_l/P$ and $p \in \{p \in \mathbb{N}^+ \mid \psi_l - 2n_{l,e}\varphi_l \leq \eta_l p \leq \psi_l - 2n_{l,s}\varphi_l\}$. Furthermore, we focus on $\mathbf{H}_{l,p}(n, k) = e^{-j2\pi(\frac{n}{N}N\epsilon_{l,p} + \frac{k}{K}f_s\tau_l)} [\Theta]_{n,k}$. Applying the shift property of 2D-IDFT, $\mathbf{X}_{l,p} = \mathbf{F}_A^H \mathbf{H}_{l,p} \mathbf{F}_D^*$ should satisfy the block sparsity with its significant entries localized within the square region

$\mathcal{A}_{l,2,p}$ with

$$\begin{aligned} \mathcal{A}_{l,2,p} = \{(n, k) \in \mathbb{Z}^2 \mid n = \text{mod}(n_{l,1} + N\epsilon_{l,p}, N), \\ k = \text{mod}(k_{l,1} + f_s\tau_l, K), \forall (n_{l,1}, k_{l,1}) \in \mathcal{A}_{l,1}\}. \end{aligned} \quad (\text{A.10})$$

Here, $\mathcal{A}_{l,1}$ is the non-zero region for $\mathbf{F}_A^H \Theta(\psi_l, \varphi_l) \mathbf{F}_D^*$, and $\text{mod}(a, m)$ is the modulus of a for m . Considering all P frequency components, the significant entries of \mathbf{X}_l would be localized within the region $\mathcal{A}_{l,2} \triangleq \bigcup_p \mathcal{A}_{l,2,p}$. Thus, the proof is completed.

REFERENCES

- [1] M. Cui, Z. Wu, Y. Lu, X. Wei, and L. Dai, "Near-field MIMO communications for 6G: Fundamentals, challenges, potentials, and future directions," *IEEE Commun. Mag.*, no. 1, Jan. 2023.
- [2] Z. Wang, J. Zhang, H. Du, D. Niyato, S. Cui, B. Ai, M. Debbah, K. B. Letaief, and H. V. Poor, "A tutorial on extremely large-scale MIMO for 6G: Fundamentals, signal processing, and applications," *IEEE Commun. Surv. Tut.*, vol. 26, no. 3, pp. 1560–1605, Jan. 2024.
- [3] Y. Liu, C. Ouyang, Z. Wang, J. Xu, X. Mu, and A. L. Swindlehurst, "Near-field communications: A comprehensive survey," *IEEE Commun. Surv. Tut.*, pp. 1–45, Oct. 2024, early access, doi: [10.1109/COMST.2024.3475884](https://doi.org/10.1109/COMST.2024.3475884).
- [4] I. Ahmed, H. Khammari, A. Shahid, A. Musa, K. S. Kim, E. De Poorter, and I. Moerman, "A survey on hybrid beamforming techniques in 5G: Architecture and system model perspectives," *IEEE Commun. Surv. Tut.*, vol. 20, no. 4, pp. 3060–3097, Jun. 2018.
- [5] 3GPP, "NR; user equipment (UE) radio transmission and reception; part 2: Range 2 standalone," 2023.
- [6] B. Wang, F. Gao, S. Jin, H. Lin, and G. Y. Li, "Spatial- and frequency-wideband effects in millimeter-wave massive MIMO systems," *IEEE Trans. Signal Process.*, vol. 66, no. 13, pp. 3393–3406, May 2018.
- [7] A. Tang, J.-B. Wang, Y. Pan, W. Zhang, Y. Chen, H. Yu, and R. C. de Lamare, "Line-of-sight extra-large MIMO systems with angular-domain processing: Channel representation and transceiver architecture," *IEEE Trans. Commun.*, vol. 72, no. 1, pp. 570–584, Jan. 2024.
- [8] A. Tang, J.-B. Wang, Y. Pan, W. Zhang, X. Zhang, Y. Chen, H. Yu, and R. C. de Lamare, "Joint visibility region and channel estimation for extremely large-scale MIMO systems," *IEEE Trans. Commun.*, vol. 72, no. 10, pp. 6087–6101, Oct. 2024.
- [9] D. Dardari and N. Decarli, "Holographic communication using intelligent surfaces," *IEEE Commun. Mag.*, vol. 59, no. 6, pp. 35–41, Jun. 2021.
- [10] K. T. Selvan and R. Janaswamy, "Fraunhofer and fresnel distances: Unified derivation for aperture antennas," *IEEE Antennas Propag. Mag.*, vol. 59, no. 4, pp. 12–15, Jun. 2017.
- [11] Z. Yuan, J. Zhang, Y. Ji, G. F. Pedersen, and W. Fan, "Spatial non-stationary near-field channel modeling and validation for massive MIMO systems," *IEEE Trans. Antennas Propag.*, Jan. 2023.
- [12] E. D. Carvalho, A. Ali, A. Amiri, M. Angelichinoski, and R. W. Heath, "Non-stationarities in extra-large-scale massive MIMO," *IEEE Wirel. Commun.*, vol. 27, no. 4, pp. 74–80, Aug. 2020.
- [13] L. Xu, L. Cheng, N. Wong, Y.-C. Wu, and H. V. Poor, "Overcoming beam squint in mmWave MIMO channel estimation: A Bayesian multi-band sparsity approach," *IEEE Trans. Signal Process.*, vol. 72, pp. 1219–1234, Feb. 2024.
- [14] Y. Zhang, X. Wu, and C. You, "Fast near-field beam training for extremely large-scale array," *IEEE Wireless Commun. Lett.*, vol. 11, no. 12, pp. 2625–2629, Dec. 2022.
- [15] Z. Hu, C. Chen, Y. Jin, L. Zhou, and Q. Wei, "Hybrid-field channel estimation for extremely large-scale massive MIMO system," *IEEE Commun. Lett.*, vol. 27, no. 1, pp. 303–307, Jan. 2023.
- [16] H. Lei, J. Zhang, H. Xiao, X. Zhang, B. Ai, and D. W. K. Ng, "Channel estimation for XL-MIMO systems with polar-domain multi-scale residual dense network," *IEEE Trans. Veh. Technol.*, Jan. 2024.
- [17] Y. Zhu, H. Guo, and V. K. N. Lau, "Bayesian channel estimation in multi-user massive MIMO with extremely large antenna array," *IEEE Trans. Signal Process.*, vol. 69, pp. 5463–5478, Sep. 2021.
- [18] H. Imori, T. Takahashi, K. Ishibashi, G. T. F. de Abreu, D. Gonzlez G., and O. Gonsa, "Joint activity and channel estimation for extra-large MIMO systems," *IEEE Trans. Wireless Commun.*, vol. 21, no. 9, pp. 7253–7270, Sep. 2022.
- [19] A. Tang, J.-B. Wang, Y. Pan, W. Zhang, Y. Chen, H. Yu, and R. C. de Lamare, "Spatially non-stationary xl-mimo channel estimation: A three-layer generalized approximate message passing method," *arXiv preprint arXiv:2403.02633*, 2024.
- [20] X. Wei and L. Dai, "Channel estimation for extremely large-scale massive MIMO: Far-field, near-field, or hybrid-field?" *IEEE Commun. Lett.*, vol. 26, no. 1, pp. 177–181, Jan. 2022.
- [21] J. Gao, C. Zhong, G. Y. Li, J. B. Soriaga, and A. Behboodi, "Deep learning-based channel estimation for wideband hybrid mmwave massive MIMO," *IEEE Trans. Commun.*, 2023.
- [22] M. Jian, F. Gao, Z. Tian, S. Jin, and S. Ma, "Angle-domain aided UL/DL channel estimation for wideband mmwave massive MIMO systems with beam squint," *IEEE Trans. Wireless Commun.*, vol. 18, no. 7, pp. 3515–3527, May 2019.
- [23] B. Wang, M. Jian, F. Gao, G. Y. Li, and H. Lin, "Beam squint and channel estimation for wideband mmWave massive MIMO-OFDM systems," *IEEE Trans. Signal Process.*, vol. 67, no. 23, pp. 5893–5908, Oct. 2019.
- [24] I.-S. Kim and J. Choi, "Spatial wideband channel estimation for mmWave massive MIMO systems with hybrid architectures and low-resolution ADCs," *IEEE Trans. Wireless Commun.*, vol. 20, no. 6, pp. 4016–4029, Feb. 2021.
- [25] M. Cui and L. Dai, "Near-field wideband channel estimation for extremely large-scale MIMO," *Sci. China Inf. Sci.*, vol. 66, no. 7, p. 172303, Jun. 2023.
- [26] H. Hou, X. He, T. Fang, X. Yi, W. Wang, and S. Jin, "Beam-delay domain channel estimation for mmwave xl-mimo systems," *IEEE J. Sel. Top. Signal Process.*, vol. 18, no. 4, pp. 646–661, May 2024.
- [27] M. Zhang, X. Yuan, and Z.-Q. He, "Variance state propagation for structured sparse Bayesian learning," *IEEE Trans. Signal Process.*, vol. 68, pp. 2386–2400, Mar. 2020.
- [28] M. Cui and L. Dai, "Channel estimation for extremely large-scale MIMO: Far-field or near-field?" *IEEE Trans. Commun.*, vol. 70, no. 4, pp. 2663–2677, Apr. 2022.
- [29] J. Lee, G.-T. Gil, and Y. H. Lee, "Channel estimation via orthogonal matching pursuit for hybrid MIMO systems in millimeter wave communications," *IEEE Trans. Commun.*, vol. 64, no. 6, pp. 2370–2386, Apr. 2016.
- [30] T. Lin, X. Yu, Y. Zhu, and R. Schober, "Channel estimation for IRS-assisted millimeter-wave MIMO systems: Sparsity-inspired approaches," *IEEE Trans. Commun.*, vol. 70, no. 6, pp. 4078–4092, Apr. 2022.
- [31] J. He, H. Wyneersch, and M. Juntti, "Channel estimation for ris-aided mmwave mimo systems via atomic norm minimization," *IEEE Trans. Wireless Commun.*, vol. 20, no. 9, pp. 5786–5797, Sep. 2021.
- [32] L. Mo, X. Lu, J. Yuan, C. Zhang, Z. Wang, and P. Popovski, "Generalized unitary approximate message passing for double linear transformation model," *IEEE Trans. Signal Process.*, vol. 71, pp. 1524–1538, Apr. 2023.
- [33] M. Luo, Q. Guo, M. Jin, Y. C. Eldar, D. Huang, and X. Meng, "Unitary approximate message passing for sparse Bayesian learning," *IEEE Trans. Signal Process.*, vol. 69, pp. 6023–6039, Sep. 2021.
- [34] W. Xu, Y. Xiao, A. Liu, M. Lei, and M.-J. Zhao, "Joint scattering environment sensing and channel estimation based on non-stationary markov random field," *IEEE Trans. Wireless Commun.*, pp. 1–1, Sep. 2023.
- [35] Y. Guo, P. Sun, Z. Yuan, C. Huang, Q. Guo, Z. Wang, and C. Yuen, "Efficient channel estimation for RIS-aided MIMO communications with unitary approximate message passing," *IEEE Trans. Wireless Commun.*, Feb. 2023.
- [36] M. E. Tipping, "Sparse Bayesian learning and the relevance vector machine," *J. Mach. Learn. Res.*, vol. 1, no. Jun, pp. 211–244, Sep. 2001.
- [37] J. Fang, Y. Shen, H. Li, and P. Wang, "Pattern-coupled sparse Bayesian learning for recovery of block-sparse signals," *IEEE Trans. Signal Process.*, vol. 63, no. 2, pp. 360–372, Nov. 2015.
- [38] M. Richards, *Fundamentals of Radar Signal Processing*. New York, NY, USA: McGraw-Hill Educ., 2005.